RESEARCH PAPERS

Acta Cryst. (1995). A**51**, 7–19

Refinement of Crystal Structure Parameters using Convergent-Beam Electron Diffraction: the Low-Temperature Phase of $SrTiO_3$

By Kenji Tsuda and Michiyoshi Tanaka

Research Institute for Scientific Measurements, Tohoku University, Sendai 980, *Japan*

(*Received* 29 *November* 1993; *accepted* 19 *May* 1994)

Abstract

The method to refine crystal structure parameters (atom positions and Debye–Waller factors) using convergent-beam electron diffraction (CBED), which is applicable to crystal structure analysis of a small specimen area down to a few nm in diameter, is studied. The line profiles of higher-order Laue-zone reflections are recorded using imaging plates. Theoretical intensities are calculated based on the dynamical theory of electron diffraction with the aid of the generalized Bethe approximation to shorten calculation time. The structural parameters are determined by fitting the experimental profiles with the theoretical ones using a nonlinear least-squares method. The present method has been applied to the low-temperature phase of $SrTiO_3$. The structural parameter or the rotation angle of the oxygen octahedron has been determined to be $\varphi = 1.12\,(4)^\circ$, which shows good agreement with that obtained from electron spin resonance experiments.

1. Introduction

Convergent-beam electron diffraction (CBED) has been established as a powerful method to uniquely determine the crystal point groups (Goodman, 1975; Buxton, Eades, Steeds & Rackham, 1976; Tanaka, Saito & Sekii, 1983; Tanaka & Terauchi, 1985; Tanaka, 1989). The reason is that the CBED method can distinguish nonpolar crystals from polar crystals because it is fully based upon dynamical diffraction. It can also identify unambiguously the space-group symmetry elements of 2_1 screw axes and glide planes owing to the conspicuous dynamical diffraction effect or the dynamical extinction appearing in kinematically forbidden reflections (Cowley & Moodie, 1959; Miyake, Takagi & Fujimoto, 1960; Cowley, Moodie, Miyake, Takagi & Fujimoto, 1961; Goodman & Lehmpfuhl, 1964; Gjønnes & Moodie, 1965). As a result, 181 space groups can be uniquely identified using only the dynamical extinction (Steeds, Rackham & Shannon, 1978; Tanaka, Sekii & Nagasawa, 1983; Tanaka & Terauchi, 1985; Tanaka, Terauchi & Kaneyama, 1988). The CBED method has been successfully applied to the symmetry determination of many materials (see *e.g.* Goodman & Whitefield, 1980; Steeds & Evans, 1980; Tanaka, Saito & Watanabe, 1980; Tanaka & Terauchi, 1985; Tanaka *et al.*, 1988; Tsuda, Tanaka, Sakanoue *et al.*, 1989; Tsuda, Tanaka & Akimitsu, 1989). In particular, symmetry changes due to very small atomic displacements at structural phase transitions have been successfully detected (Tanaka, Saito & Tsuzuki, 1982; Tanaka, Sekii & Ohi, 1985; Tanaka & Terauchi, 1985; Tanaka *et al.*, 1988), which led us to believe that the CBED method has the potential to determine very small atomic displacements. Recently, application of CBED has been extended to the symmetry determination of higher-dimensional crystals or incommensurately modulated crystals (Terauchi & Tanaka, 1993; Tanaka, 1994; Terauchi, Takahashi & Tanaka, 1994) and quasicrystals (Tanaka, Terauchi, Hiraga & Hirabayashi, 1985; Bendersky & Kaufman, 1986; Saito, Tanaka, Tsai, Inoue & Masumoto, 1992; Tanaka *et al.*, 1993).

The symmetry determination described above is a qualitative use of the CBED method. CBED is now entering a stage of quantitative studies, or crystal structure analysis. The CBED method has the following advantages compared with the X-ray and neutron diffraction methods with respect to crystal structure analysis. Firstly, the CBED method enables us to obtain diffraction patterns from a small specimen area a few nm in diameter. The area illuminated by an incident electron beam is small enough for a crystal to be expected to be perfect and to have a constant thickness and orientation. Consequently, the CBED patterns can be directly compared with calculated ones based on the dynamical theory of electron diffraction. Then, the method can be applied not only to the determination of perfect crystal structures but also to that of local crystal structures that change with specimen position. This is contrasted with the fact that the X-ray and neutron diffraction analyses determine the structural parameters averaged over a large specimen volume, which consists of mosaic crystals and includes many lattice defects. Secondly, the CBED intensities possess information about the

© 1995 International Union of Crystallography
Printed in Great Britain – all rights reserved

ISSN 0108-7673 ©1995

phases of crystal structure factors because of the strong dynamical diffraction effects. This is very different from the X-ray and neutron diffraction cases, in which the intensities are calculated on the basis of the kinematical diffraction theory and have no information about phases of crystal structure factors.

The earliest attempt at crystal structure analysis using electron diffraction was conducted by Vainshtein and co-workers (Vainshtein, 1956, 1964; Vainshtain, Zvyagin & Avilov, 1992). They took note of the fact that the contribution of light elements in electron diffraction is greater than that in X-ray diffraction, and applied the electron diffraction method to the analysis of materials including light elements. They took diffraction patterns from specimens with lamellar and/or fibrous textures and evaluated the diffracted intensities recorded on negative films by visual estimation. They also determined crystal structures using the Fourier synthesis method based on the kinematical diffraction theory. Dorset (1992) applied the direct phasing method of X-ray crystallography to the Fourier synthesis of the electron diffraction data, and determined the structures of layer silicates and thiourea. Vincent, Bird & Steeds (1984) first applied the CBED method to the determination of the atom positions of AuGeAs. They evaluated the experimental intensities from negative films by visual estimation. They refined the positional parameters by fitting the experimental intensities of higher-order-Laue-zone (HOLZ) reflections with the intensities calculated under the quasikinematical approximation. Vincent & Exelby (1990) applied the same method to the structure determination of a metastable Al–Ge phase. Other attempts to refine positional or occupational parameters have been made by Taftø & Metzger (1985), Vincent & Bird (1986), Gjønnes, Boe & Gjønnes (1990) and Tomokiyo & Kuroiwa (1990). All of the above analyses were based on the kinematical or quasikinematical diffraction theory. We are convinced from our experience that it is necessary to use the dynamical diffraction theory for accurate matching of experimental and calculated intensities, even for HOLZ reflections. Tanaka & Tsuda (1990, 1991) preliminarily refined the structural parameters of the low-temperature phase of $SrTiO_3$, by applying the dynamical theory of electron diffraction for the first time.

Recently, the automatic matching of experimental and theoretical CBED patterns has been attempted by minimization of an R factor by a nonlinear least-squares method: a steepest-descents method (Marthinsen, Høier & Bakken, 1990), the simplex method (Zuo & Spence, 1991), the quasi-Newtonian method (Bird & Saunders, 1991) and the modified Marquardt method (Tanaka & Tsuda, 1991). Bird & Saunders (1992*a*,*b*) studied the sensitivity and accuracy of the matching of CBED patterns and tested an *ab initio* determination method of the structure factors of GaP using simulated patterns as ideal experimental data. For the refinement of low-order structure factors, readers should refer to a review paper by Spence (1993).

Important requirements for accurate structure analysis using the CBED method are as follows. The first is *accurate intensity measurements*. Electron diffraction intensities have for a long time been recorded by negative film. This film is not suitable for quantitative intensity measurements because of its narrow dynamic range and its nonlinear response to electron doses. Recently, new recording tools, which have great sensitivity, wide dynamic range and a linear response to electron doses, have been developed: a slow-scan charge-coupled-device (CCD) camera (Mochel & Mochel, 1986; Mooney, Fan, Meyer, Truong & Krivanek, 1990) and an imaging plate (IP) (Mori, Oikawa, Kato, Miyahara & Harada, 1988; Mori, Oikawa, Harada & Miyahara, 1990; Oikawa, Mori, Takano & Ohnishi, 1990). We have introduced an imaging-plate system to record accurately the intensities of CBED patterns. The second requirement is *subtraction of inelastically scattered electrons*. It is important to subtract inelastically scattered intensities to obtain accurate experimental data for comparison with calculated intensities. It has been said that phonon scattering was worse than plasmon scattering because the former causes interband transitions but the latter causes intraband transitions. However, Tanaka & Tsuda (1991) demonstrated for silicon and FeS_2 using a sector-type energy-filter that subtraction of plasmon-loss electrons from the experimental intensity is very important to obtain the pattern to be compared with theoretical calculations, and that phonon scattering appears to spoil the pattern very little. Recently, a commercial electron microscope equipped with an omega-type energy filter in its column to cut off plasmon-loss electrons has become available (Mayer, Spence & Möbus, 1991). A practical way to remove the inelastic part without an energy filter is to subtract the intensity just outside the CBED disc from that inside the disc. It is also effective to use a thin specimen to reduce the inelastic scattering. The third requirement is *high-speed dynamical calculations*. Many-beam dynamical calculation using more than a hundred beams is necessary to obtain accurate CBED intensities. It includes the diagonalization of a square matrix with the size of the beam number, which takes a long calculation time. To obtain one-dimensional line profiles or two-dimensional patterns, the intensity calculations have to be carried out for a large number of points with different excitation errors or different directions of electron incidence. Furthermore, such calculations have to be repeated with changing structural parameters in obtaining the final values of the parameters using the nonlinear least-squares method. Such calculations require a very long computing time but recently have become faster due to rapid development of workstations. Techniques to shorten computing time are, however, still important, such as the generalized-Bethe-

potential method and a perturbation method to calculate the gradients of the residual sum of squares required in the nonlinear least-squares method.

Considering the above points, we have developed a method to refine crystal structure parameters (atom positions and Debye–Waller factors) and applied it to the positional-parameter determination of the low-temperature phase of $SrTiO_3$. In §2, the procedure of crystal structure analysis is described. In §3, the result of application of the method to the low-temperature phase of $SrTiO_3$ is reported. In §4, we compare the results with other experimental studies and give an interpretation of HOLZ line profiles in terms of the Bloch-wave scheme. Some future problems are mentioned in §5.

2. Analysis procedure

We describe the analysis procedure of the present method. There are two major premises. One is the use of *HOLZ reflections*. Generally, intensities of HOLZ reflections with large reciprocal vectors **g** are more sensitive to the displacements of atoms than those of zeroth-order-Laue-zone (ZOLZ) reflections. This can be understood from the fact that the crystal structure factor F_g contains the phase factor $\exp(-2\pi\mathbf{g}\cdot\mathbf{r})$. For a reflection with a large **g**, the phase factor varies greatly through small changes of atomic coordinates **r**. Then, small displacements of atoms can be sensitively detected using HOLZ reflection intensities. The other premise is the use of *line profiles*. Intensity distributions of HOLZ reflections in CBED patterns have characteristic structures, which are attributed to the structures of dispersion surfaces of Bloch waves. Then, more information can be obtained by treating intensities of HOLZ reflections as one-dimensional line profiles or two-dimensional intensity distributions than as integrated intensities. Although it is best to treat those as two-dimensional data, we use one-dimensional line profiles to reduce computing time of dynamical calculations. It is noted that intensities of HOLZ reflections are almost uniform over a limited extent in the azimuthal direction when a CBED pattern is taken from a thin specimen area.

In advance of the analysis, the space group, the lattice parameters and the tentative positional parameters of atoms of a specimen and the accelerating voltage of the incident electrons are assumed to be known. The accelerating voltage is determined from a HOLZ line pattern of a standard specimen like silicon. The analysis procedure is as follows:

(i) A CBED pattern is taken from the specimen using the IP in the electron microscope. A thin area of the specimen has to be chosen to reduce inelastically scattered intensities. If the expected atomic displacements are known, a direction of the electron incidence is selected so that the CBED pattern is sensitive to the displacements.

(ii) Intensities of the CBED pattern are read out from the IP by the IP reader and are transferred to the workstation as a digital image.

(iii) The distortion of the pattern owing to the lens aberrations of the electron microscope is numerically corrected on the workstation. Line profiles of HOLZ reflections that run along the radial directions through the centers of the discs are taken from the CBED pattern.

(iv) The thickness of the specimen is evaluated by comparing the patterns of low-order ZOLZ reflections with those simulated at different thicknesses. Since the patterns are not so sensitive to the detail of the structure, the dynamical simulations are carried out using the structural parameters initially assumed.

(v) The structural parameters are refined by the nonlinear least-squares method so as to minimize the residual sum of squares S between the experimental HOLZ line profiles and calculated ones.

Details of each process are described in the following subsections.

2.1. *Intensity measurements*

2.1.1. *Use of imaging plates.* We have used imaging plates of Fuji DL-UR III and an IP system (JEOL PIXsysTEM) to record CBED patterns. The IP has a great sensitivity, a wide dynamic range of four digits (10^{-14} – $10^{-9}\,\mathrm{C\,cm^{-2}}$) and a linear response with electron dose. A disadvantage of the IP is its low spatial resolution. It was measured to be about 120 μm at 1000 kV by Isoda, Saitoh, Moriguchi & Kobayashi (1991), while it is about 10 μm for negative films. This disadvantage, however, can be compensated for by taking CBED patterns with a high magnification. The IP system is composed of IPs, an IP camera, an IP reader and a workstation. The IPs are set into the IP camera in the electron microscope and exposed to electrons to record CBED patterns. The recorded pattern is read out by the IP reader using an He–Ne laser beam, and transferred to the workstation as a digitized pattern with 4096 logarithmic signal levels and 2048 × 1536 pixels.

It is worth comparing the IP with the slow-scan CCD camera. The CCD camera, which has also been recently developed as a new recording tool, has a similar performance to the IP system with respect to sensitivity, dynamic range and linear response. The advantage of the CCD is on-line use, while the IP is used off-line. The CCD, with a size of 25.4 × 25.4 mm, may be a little small to record the entire CBED pattern including HOLZ reflections with one exposure. If the entire CBED pattern is recorded on the CCD at a short camera length, an appreciable distortion owing to the aberration of intermediate and projector lenses can take place in

current electron microscopes. The IP, with a size of 77×102 mm, is almost free of such distortion and is better for recording CBED patterns.

2.1.2. *HOLZ line profiles.* Line profiles of HOLZ reflections that run along radial directions through the centers of the HOLZ discs are taken out of the recorded pattern on the workstation. Relative positions of HOLZ reflection discs or their line profiles have to be measured accurately, because those positions seriously affect the accuracy of the result for the profile fitting. The positions are calculated with the basis vectors of ZOLZ reflections and indices of the HOLZ reflections because the discs of HOLZ reflections are difficult to see, unlike those of ZOLZ reflections.

For the accurate determination of positions of the line profiles, it is necessary to correct the distortion of the CBED pattern due to aberrations of the intermediate lens and the projection lens of the electron microscope. Even at the optimum settings of the lenses and the stigmators, the distortions cannot be completely eliminated in current electron microscopes. The distortion consists of radial distortion and spiral distortion (*e.g.* Tsuno & Harada, 1981; Reimer, 1989). The radial distortion is caused by the aberrations of both the intermediate lens and the projector lens and results in a displacement of the pattern in the radial direction. The spiral distortion originates from the projector lens and causes a displacement in the azimuthal direction. The displacements Δr of the radial distortion and Δs of the spiral distortion are expressed by $\Delta r = C_r r^3$ and $\Delta s = C_{sp} r^3$, where r is the distance from the optical axis, and C_r and C_{sp} are the coefficients of the radial and spiral distortions, respectively. The two types of distortion are corrected using the equations on the workstation.

CBED patterns taken from thin areas (<300 Å) of a specimen still contain inelastic background intensity. In the present analysis, the remaining background intensity was determined from the intensities just outside the CBED discs by a linear interpolation and was subtracted from the total intensity.

HOLZ reflection intensities for thin specimens are almost uniform over a certain extent in the azimuthal direction, but the effect of azimuthal intensity variation is indirectly taken into account through the weight factors w_{gi} of the reflections in the least-squares fitting of the line profiles. We took out two additional line profiles that were separated by a few pixels on both sides of the former one and calculated the averaged values and the standard deviations σ_{gi} of the three line profiles. The averaged values were used as experimental intensities. The standard deviations σ_{gi} were regarded as experimental errors and the weight factors w_{gi} were taken to be $1/\sigma_{gi}^2$. This implies that, when the standard deviation of a reflection is large, or the reflection has a large azimuthal intensity variation, the weight factor w_{gi} is set to be small in the least-squares fitting.

2.2. *Calculations*

2.2.1. *Dynamical calculations.* Theoretical intensities of CBED patterns are obtained by many-beam dynamical calculations. We wrote a Fortran program for the calculation based on the Bloch-wave dynamical theory of electron diffraction (Bethe, 1928). The Bloch-wave theory, which has been described in many texts and reviews (*e.g.* Hirsch, Howie, Nicholson, Pashley & Whelan, 1977; Jones, Rackham & Steeds, 1977), is briefly described as follows. The Schrödinger equation for the wave function $\Psi(\mathbf{r})$ of an electron within a crystal potential $V(\mathbf{r})$ is expressed by

$$\nabla^2\Psi(\mathbf{r}) + (8\pi me/h^2)[E + V(\mathbf{r})]\Psi(\mathbf{r}) = 0, \quad (1)$$

where m is the relativistic mass of the electron and E is the accelerating voltage of the incident electron. The crystal potential $V(\mathbf{r})$ and the wave function $\Psi(\mathbf{r})$ can be expanded as a Fourier series of the reciprocal-lattice vector $\mathbf{g}$:

$$V(\mathbf{r}) = \sum_g V_g \exp(2\pi i \mathbf{g}\cdot\mathbf{r}) \quad (2)$$

and

$$\Psi(\mathbf{r}) = \sum_g C_g(\mathbf{k}) \exp[2\pi i(\mathbf{k}+\mathbf{g})\cdot\mathbf{r}]. \quad (3)$$

Substituting (2) and (3) into (1) and comparing coefficients of each exponential term, we obtain the basic equation of the Bloch-wave theory:

$$\left[\mathbf{K}^2 - (\mathbf{k}+\mathbf{g})^2\right]C_g(\mathbf{k}) + \sum_{h\neq g} U_h C_{g-h}(\mathbf{k}) = 0, \quad (4)$$

where $\mathbf{K}^2 = (E + V_0)2me/h^2$ and $U_g = 2meV_g/h^2$. This is an eigenvalue equation and can be solved numerically. Then, the amplitude of the jth Bloch wave is expressed by the jth eigenvalue $\mathbf{k}^{(j)}$ and the jth eigenvectors $C_g^{(j)}(\mathbf{k})$ as follows:

$$\Psi^{(j)} = \sum_g C_g^{(j)}(\mathbf{k}) \exp\left[2\pi i(\mathbf{k}^{(j)}+\mathbf{g})\cdot\mathbf{r}\right]. \quad (5)$$

The wave function of the electron inside the crystal is expressed as a linear combination of the Bloch waves. The diffracted amplitude Ψ_g and intensity I_g of the reflection g are given by

$$\Psi_g = \sum_j \varepsilon^{(j)} C_g^{(j)}(\mathbf{k}) \exp\left(2\pi i k_z^{(j)} t\right) \quad (6)$$

and

$$I_g = \Psi_g^* \Psi_g, \quad (7)$$

where $\varepsilon^{(j)}$ is the excitation amplitude of the jth Bloch

wave and is determined by the boundary condition at the upper surface of the specimen, and t is the specimen thickness. A simulated CBED pattern is obtained by calculating I_g with changing incident electron direction.

Our dynamical calculation program uses the subroutine *CHEQRS* in *NUMPAC* (Nagoya University Mathematical Libraries, Nagoya, Japan) to find the eigenvalues and eigenvectors of a general complex matrix and the routine *MINVC*2 in *NUMPAC* to find the inverse of the matrix of eigenvectors.

Absorption due to inelastic scattering is taken into account using an absorption (imaginary) potential. The absorption consists of two parts: anomalous absorption and mean absorption. The anomalous absorption arises from scattering processes due to localized objects such as thermal diffuse scattering (TDS) and core-electron excitations. TDS is the most significant process and causes the main contribution to the Fourier coefficients with $\mathbf{g} \neq 0$ of the imaginary potential. On the other hand, the mean absorption arises from nonlocal scattering such as plasmon excitations and interband excitations. The mean absorption is not important for the present study because it causes only uniform attenuation of all reflections. The theory used to calculate the TDS contribution to the absorption potential was given by Hall & Hirsch (1965) and uses the Einstein model of lattice vibrations. Bird & King (1990) computed the TDS contributions in the form of the absorptive part to the atomic form factor and incorporated them into the Fortran subroutine *ATOM*. We have employed the imaginary potential calculated using the subroutine *ATOM*.

2.2.2. *Generalized Bethe-potential method.* The Bethe-potential (BP) method (Bethe, 1928; Gjønnes, Gjønnes, Zuo & Spence, 1988; Zuo, Spence & Høier 1989) was introduced to estimate the influence of weakly excited beams on a strongly excited beam. We have applied the generalized-Bethe-potential (GBP) method, which was proposed for reflection electron diffraction by Ichikawa & Hayakawa (1977) to reduce the dynamical calculation time. The GBP method gives more accurate intensities than the BP method because the former includes all the higher-order Bethe-potential terms neglected in the latter. In the GBP method, diffracted beams are classified into 'weakly excited' and 'strongly excited' beams in the same manner as in the BP method. Then, the effects of weakly excited beams are incorporated into the crystal-potential coefficients of strongly excited beams and the order of the matrix is reduced to the number of strongly excited beams. The formulation of the GBP method is described next.

We consider, for simplicity, a four-beam case, which is easily extended to n-beam cases. We assume beams 1 and 2 to be 'strongly excited' and beams 3 and 4 to be 'weakly excited'. The basic equation [(4)] of the Bloch-wave dynamical theory is expressed by a 4×4 matrix

$$\begin{bmatrix} K^2 - k_0^2 & U_{0-1} & U_{0-2} & U_{0-3} \\ U_{1-0} & K^2 - k_1^2 & U_{1-2} & U_{1-3} \\ U_{2-0} & U_{2-1} & K^2 - k_2^3 & U_{2-3} \\ U_{3-0} & U_{3-1} & U_{3-2} & K^2 - k_3^2 \end{bmatrix} \begin{bmatrix} C_0 \\ C_1 \\ C_2 \\ C_3 \end{bmatrix} = 0, \qquad (8)$$

where $\mathbf{k}_g$ means $\mathbf{k} + \mathbf{g}$. Equation (8) is divided into two parts: the upper half

$$\begin{bmatrix} K^2 - k_0^2 & U_{0-1} \\ U_{1-0} & K^2 - k_1^2 \end{bmatrix} \begin{bmatrix} C_0 \\ C_1 \end{bmatrix} = - \begin{bmatrix} U_{0-2} & U_{0-3} \\ U_{1-2} & U_{1-3} \end{bmatrix} \begin{bmatrix} C_2 \\ C_3 \end{bmatrix} \qquad (9)$$

and the lower half

$$\begin{bmatrix} K^2 - k_2^2 & U_{2-3} \\ U_{3-2} & K^2 - k_3^2 \end{bmatrix} \begin{bmatrix} C_2 \\ C_3 \end{bmatrix} = - \begin{bmatrix} U_{2-0} & U_{2-1} \\ U_{3-0} & U_{3-1} \end{bmatrix} \begin{bmatrix} C_0 \\ C_1 \end{bmatrix}. \qquad (10)$$

Eliminating C_2 and C_3 from (9) and (10), we obtain

$$\left\{ \begin{bmatrix} K^2 - k_0^2 & U_{0-1} \\ U_{1-0} & K^2 - k_1^2 \end{bmatrix} - \begin{bmatrix} U_{0-2} & U_{0-3} \\ U_{1-2} & U_{1-3} \end{bmatrix} \times \begin{bmatrix} K^2 - k_2^2 & U_{2-3} \\ U_{3-2} & K^2 - k_3^2 \end{bmatrix}^{-1} \begin{bmatrix} U_{2-0} & U_{2-1} \\ U_{3-0} & U_{3-1} \end{bmatrix} \right\} \times \begin{bmatrix} C_0 \\ C_1 \end{bmatrix} = 0. \qquad (11)$$

The second term within the braces of (11) is the term incorporating the effect of the weakly excited beams into the strongly excited beams. The term is evaluated using an approximation to replace $\mathbf{k}$ with $\mathbf{K}$. This approximation corresponds to the replacement of the eigenvalue k of a Bloch wave, which should be obtained by solving the eigenvalue equation (8), with the incident wave vector $\mathbf{K}$ inside the crystal. Thus, the order of the matrix (11) to be diagonalized is reduced to 2×2. The GBP method is very effective for shortening calculation time with good precision, when it is applied to a pattern that includes a number of weak beams. We treat ZOLZ reflections with large $\mathbf{g}$ and large excitation errors as 'weakly excited' beams, which appear at the outer part of a CBED pattern taken at an electron incidence parallel to a high-symmetry zone axis.

2.2.3. *Nonlinear least-squares fitting.* The structural parameters are refined so as to minimize the residual sum of squares S between the experimental HOLZ line profiles and the calculated ones. The quantity S is

defined as

$$S = \sum_g \sum_i w_{gi} \left[I_{gi}^{\rm obs} - s I_{gi}^{\rm cal}(\mathbf{x}) \right]^2, \tag{12}$$

where $I_{gi}^{\rm obs}$ is the ith intensity of the line profile of reflection g, $I_{gi}^{\rm cal}$ is the calculated intensity corresponding to $I_{gi}^{\rm obs}$ with the structural parameters $\mathbf{x}$, w_{gi} are weight factors and s is a scale factor common to all the calculated intensities. We have assumed the weight factors $w_{gi} = 1/\sigma_{gi}^2$, where σ_{gi} is the experimental error of $I_{gi}^{\rm obs}$ and is evaluated as described in §2.1.2. Minimization of S is performed by the modified Marquardt method (Fletcher, 1971), which is implemented in the Fortran program *SALS* (statistical analysis with least-squares fitting) (Nakagawa & Oyanagi, 1980). The method has characteristics of both the steepest-descents method and the Gauss–Newton method. It works like the steepest-descents method in regions where the parameters show nonlinear behavior and like the Gauss–Newton method in regions where the parameters show linear behavior. The fitting starts from a set of initial values of the structural parameters and continues until S reaches a minimum. An appropriate choice of the initial values is necessary in obtaining the global minimum of S or the correct solution, because spurious minima of S can exist in the multidimensional space of the parameters. It is thus necessary to repeat the fitting using several different sets of initial values.

Similar to conventional X-ray structure analysis, the reliability factors

$$R = \sum_i \left| I_i^{\rm obs} - s I_i^{\rm cal} \right| / \sum_i I_i^{\rm obs} \tag{13}$$

and

$$R_w = \left\{ \left[\sum_i \left(I_i^{\rm obs} - s I_i^{\rm cal} \right)^2 / \sigma_i^2 \right] \left(\sum_i I_i^{\rm obs\,2} / \sigma_i^2 \right)^{-1} \right\}^{1/2} \tag{14}$$

are calculated, where $I_i^{\rm obs}$ is the ith observed intensity, $I_i^{\rm cal}$ is the ith calculated intensity and s is a scale factor.

The standard deviations of the refined parameters are evaluated according to the error-propagation rule as follows: The error matrix Σ of observed data is defined as

$$\Sigma = \begin{bmatrix} \sigma_1^2 & & 0 \\ & \ddots & \\ 0 & & \sigma_n^2 \end{bmatrix}, \tag{15}$$

where σ_i is the standard deviation of the ith observed data. Jacobian A is the matrix of partial differential coefficients of the model function f with respect to a fitting parameter, and its ij element is written as

$$A_{ij} = \partial f / \partial x_i. \tag{16}$$

From Σ and A, the error matrix $\Sigma_{\widehat{x}}$ of the refined parameters $\widehat{x}$ is given by

$$\Sigma_{\widehat{x}} = \left(\widetilde{A} \Sigma^{-1} A \right)^{-1}, \tag{17}$$

where the tilde indicates the transpose of the matrix. Equation (17) is called the error-propagation rule. By it, the standard deviations of the refined parameters $\widehat{x}$ are obtained as the square root of each diagonal element of $\Sigma_{\widehat{x}}$.

3. Application to $SrTiO_3$

3.1. *The low-temperature phase of* $SrTiO_3$

We have applied the present method to the low-temperature phase of $SrTiO_3$. $SrTiO_3$ undergoes a second-order phase transformation at 105 K from the high-temperature phase of space group *Pm*3*m* to the low-temperature phase of space group *I*4/*mcm* (Unoki & Sakudo, 1967). The high-temperature phase has the cubic perovskite structure, in which the oxygen octahedron contains a Ti atom at its center. In the low-temperature phase, the oxygen octahedron rotates slightly, owing to the condensation of the R_{25}-phonon mode of the high-temperature phase. The positions of Sr and Ti atoms are unchanged. The lattice parameters a and c of the low-temperature phase and a_c of the high-temperature phase are related by $a \simeq 2^{1/2} a_c$ and $c \simeq 2a_c$. Table 1 shows the atomic coordinates of the low-temperature phase. The crystal structure of the low-temperature phase projected along the [001] axis is shown in Fig. 1. The rotation angle φ of the oxygen octahedron is related to the parameter x of the O(2) atoms by the equation $x = (1 - \tan\varphi)/4$. Therefore, the structure analysis of the low-temperature phase allows one to determine the

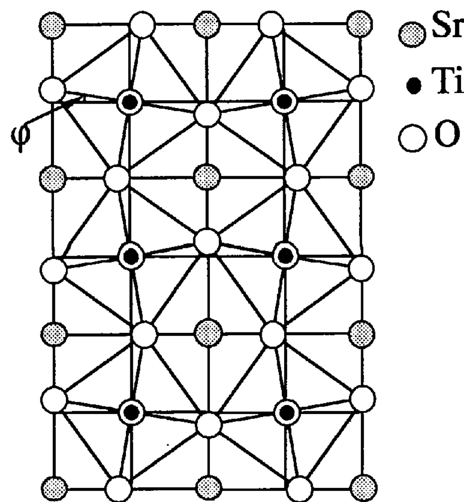

Fig. 1. Crystal structure of the low-temperature phase of $SrTiO_3$ projected along the [001] axis.

Table 1. *Atomic coordinates of the low-temperature phase of* $SrTiO_3$

Atom	Wyckoff position	x	y	z
Sr	4(*b*)	0	1/2	1/4
Ti	4(*c*)	0	0	0
O(1)	4(*a*)	0	0	1/4
O(2)	8(*h*)	x	$1/2+x$	0

rotation angle φ of the octahedron and the Debye–Waller factor B of the oxygen ions, where B is assumed to be isotropic. $SrTiO_3$ is the most suitable substance for the first application of the present method.

3.2. *Experimental*

Terauchi (1988) examined crystal space groups of three kinds of specimens grown by the flux, Czochralski and Verneuil methods, using the CBED method, and reported that only the specimens grown by the flux method clearly showed the space group *I4/mcm* but the other two did not give the space group due to residual lattice strain. Then, the bulk specimen of $SrTiO_3$ produced by the flux method was used in the present experiments. The thin-film specimens for transmission electron microscopy were prepared by chemical polishing using phosphoric acid heated at about 473 K. CBED experiments were conducted using a JEOL 100CX transmission electron microscope equipped with a field-emission gun, an IP system and a liquid-nitrogen cooling specimen holder.

We chose the [001] zone axis as the electron-beam incidence because the displacements of O(2) atoms due to the phase transformation take place in the (001) plane.

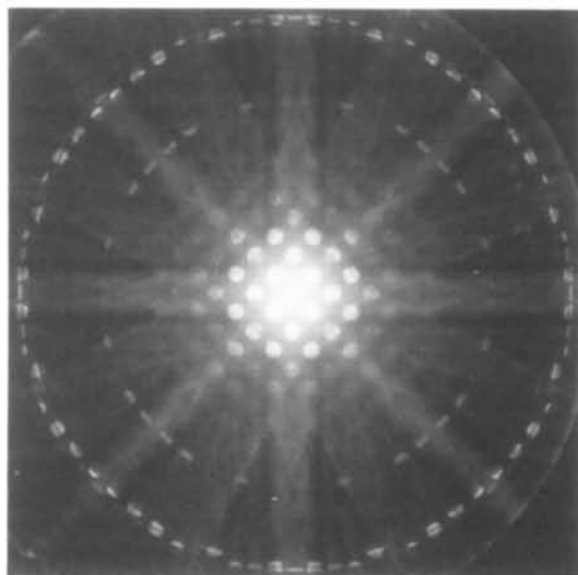

Fig. 2. CBED pattern of the low-temperature phase of $SrTiO_3$, taken from a 3 nm-diameter area with [001] incidence at 87 K. Total symmetry of the pattern is 4*mm*.

Fig. 2 shows a CBED pattern of the low-temperature phase taken with the [001] incidence at 87 K. The pattern was obtained from a 3 nm-diameter area in a domain although minute twin domains were introduced in the low-temperature phase. It should be noted that the X-ray and neutron diffraction techniques cannot obtain diffraction intensities from a single domain. ZOLZ reflections are seen in the center of the pattern. HOLZ reflections appear as rings surrounding the ZOLZ reflections. It should be noted that the first-order-Laue-zone (FOLZ) reflections are superlattice reflections appearing only in the low-temperature phase and are sensitive to the rotation of the oxygen octahedron. The CBED pattern exhibited fourfold rotation and two types of mirror symmetry, total symmetry of the pattern being 4*mm*. Then, the reflections within a one-eighth sector are independent with respect to symmetry operations.

After the distortion correction and averaging of the CBED pattern, described in §2.1.2, line profiles of the symmetry-independent reflections were taken out of the CBED pattern. Background intensities with a linear form were subtracted from each line profile using the intensities at both ends of the line profile. The ratio of inelastic to elastic parts was approximately 20% in the FOLZ reflections and 10% in the SOLZ (second-order Laue zone) ones at the line profiles. The inelastic background arises mainly from plasmon scattering and thermal diffuse scattering (TDS). Since electrons suffering from plasmon scattering form intensity profiles similar (but not identical) to those of elastic electrons, the linear interpolation is a first approximation. However, it looks like a reasonable approximation because the contribution of plasmon scattering in $SrTiO_3$ was confirmed to be smaller than that of metals from a separate experiment using an energy analyzer. On the other hand, electrons suffering from TDS spread over large scattering angles, some forming Kikuchi lines and Kikuchi bands. Background intensities due to TDS are well approximated by a linear interpolation, except in the areas of Kikuchi lines and Kikuchi band edges. For these reasons, the procedure of background subtraction appears to produce little error in the present analysis.

3.3. *Determination of the accelerating voltage and the specimen thickness*

The accelerating voltage of the electron microscope was determined using a HOLZ line pattern of silicon as a standard specimen. Fig. 3 shows the CBED pattern of the bright-field disc of silicon taken with the [111] incidence at a nominal accelerating voltage of 80 kV. Six distances A, B, C, D, E and F were measured and the ratios between these distances compared with those of a series of dynamically simulated CBED patterns for different accelerating voltages, where the specimen thickness was not necessarily exact but adequate if the observed pattern was roughly reproduced. It is empha-

sized that not kinematical but dynamical simulation is necessary for the accurate determination of the voltage because the HOLZ line positions shift from those given by kinematical approximation owing to the dynamical diffraction effect. The HOLZ line shifts reach amounts corresponding to accelerating voltages of several kV. Then, the accelerating voltage was determined to be 86.0 (3) kV.

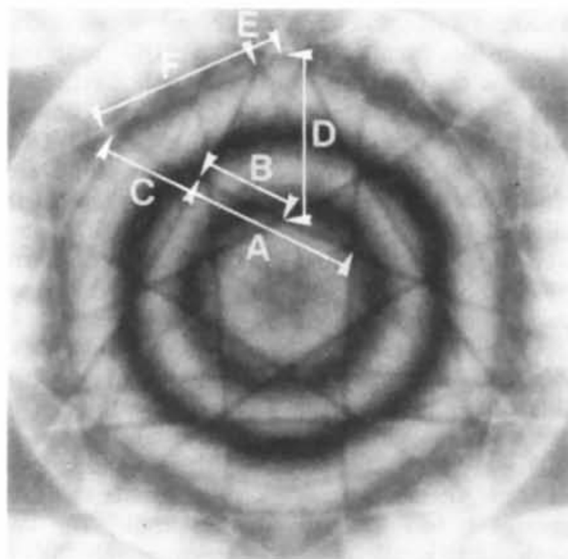

Fig. 3. CBED pattern of the bright-field disc of silicon taken with [111] incidence at a nominal accelerating voltage of 80 kV. Six distances *A*, *B*, *C*, *D*, *E* and *F* were measured to determine the accelerating voltage of the electron microscope. The actual accelerating voltage was determined to be 86.0 (3) kV from the fitting of these distances with those in dynamically simulated patterns.

The specimen thickness was determined by comparing the experimental ZOLZ CBED pattern with calculated ones. Fig. 4(*a*) shows the central part of Fig. 2, the ZOLZ CBED pattern. Figs. 4(*b*)–(*d*) show three patterns from a series of dynamically simulated patterns for different specimen thicknesses, where the accelerating voltage of 86 kV obtained was used, and a rotation angle φ for the oxygen octahedron of 1.4° and the Debye–Waller factor for O(2) of 0.4 Å^2 were assumed. It is noted that the ZOLZ CBED pattern is not so sensitive to the values of φ and B. Close comparison of Fig. 4(*a*) and Figs. 4(*b*)–(*d*) determined the specimen thickness to be 200 (10) Å.

3.4. *Sensitivity of HOLZ line profiles*

We carried out in advance test simulations of the HOLZ line profiles with varying φ and B to examine the sensitivity of HOLZ line profiles to φ and B[O(2)]. Fig. 5(*a*) shows simulated line profiles of the 7,12,1 FOLZ reflection for different rotation angles φ, where the values of B and t, the specimen thickness, were fixed at 0.3 Å^2 and 250 Å, respectively. Considerable intensity changes are seen to occur with small changes in φ. Fig. 5(*b*) shows simulated 7,12,1 line profiles for

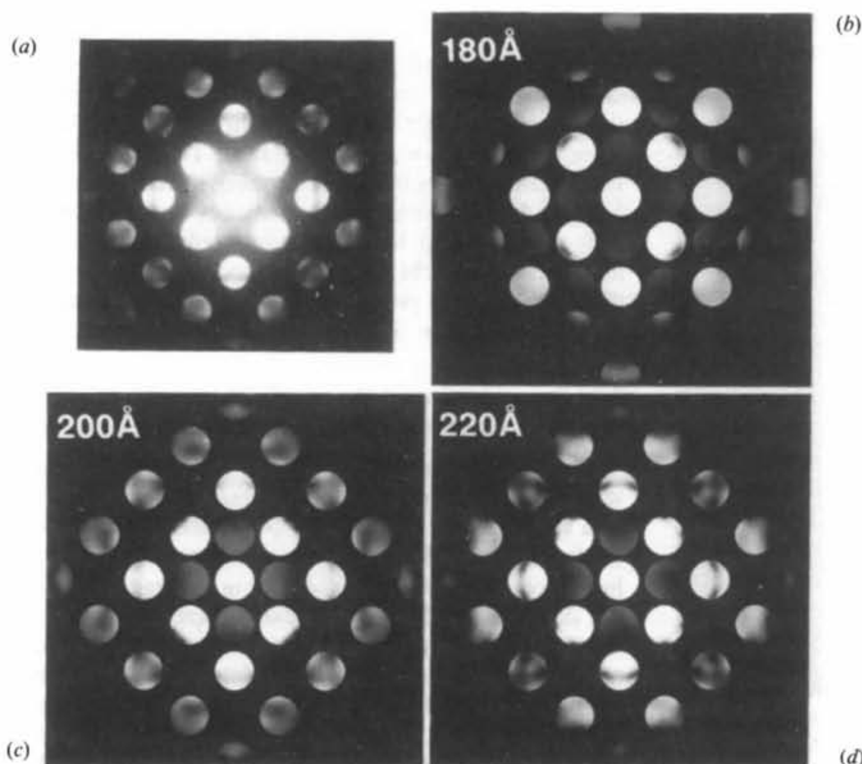

Fig. 4. ZOLZ CBED patterns: (*a*) an experimental pattern (the central part of Fig. 2); (*b*), (*c*), (*d*) dynamically simulated patterns with specimen thicknesses of 180, 200 and 220 Å, respectively. The thickness was determined to be 200 (10) Å.

different values of the Debye–Waller factor B, with φ and t set to 1.5° and 250 Å, respectively. It is also seen that the profiles show good sensitivity to the changes of B. The simulations have shown the following. Intensities of the FOLZ line profiles increase with increasing φ and decrease with increasing B. On the other hand, intensities of the $hk2$ (h, k even) SOLZ line profiles decrease with increasing φ and decrease with increasing B faster than those of the FOLZ reflections, while those of the other SOLZ ones (h, k odd) are less affected by φ and B. Therefore, it is possible to determine the parameters φ and B with sufficient accuracy using only relative intensities of the FOLZ and SOLZ line profiles.

The line profiles do not change their peak positions but their intensities. These indicate that the values of φ and B can be determined from the integrated intensities of the profiles as well as the line profiles.

3.5. *Results*

From the results in §3.4, we selected three FOLZ reflections (7,12,1, 1,14,1 and 3,14,1) and five SOLZ reflections with $hk2$ (h, k even) (14,14,2, 8,18,2, 12,16,2, 0,20,2 and 2,20,2) for the analysis. These reflections are seen in Fig. 6, which is a quarter sector of Fig. 2. These reflections appear to be uniform in intensity in the azimuthal direction. It is noted that the SOLZ reflections $hk2$ (h, k odd), whose intensities are strongly dependent on Sr and Ti, show intensity variation in the azimuthal direction. From the results of the convergence tests of HOLZ intensities with the numbers of ZOLZ and HOLZ reflections, 109 ZOLZ beams and 25 HOLZ beams were chosen for the dynamical calculations. 40 beams among the 109 ZOLZ beams were treated as weak beams when applying the GBP method. Lattice parameters used were a = 5.511 and c = 7.796 Å at 87 K (Alefeld, 1969). Debye–Waller factors of the Ba, Ti and O(1) atoms were assumed to be B(Ba) = 0.19, B(Ti) = 0.15 and B[O(1)] = 0.19 Å^2 at 87 K (Stirling, 1972).

The analyses were conducted in two ways; one dealing with the integrated intensities and the other with the line profiles. Both calculations took about 17 h on a workstation (Sony NEWS-3460) with a calculation speed of 2.7 MFLOPS.

3.5.1. *Case* I. *Integrated intensities.* From the integrated intensities of the HOLZ line profiles, the rotation angle of the oxygen octahedron φ and the Debye–Waller factor B[O(2)] were determined to minimize the residual sum of squares S between experimental intensities and calculated ones. The intensities integrated along the line profiles were used as the integrated intensities. The values obtained were φ = 1.12 (4)° and B[O(2)] = 0.35 (6) Å^2. Table 2 shows the final result of the fitting between experimental intensities and calculated ones. It is seen that the calculated intensities agree very well with the experimental ones. The R factors are R = 8.2% and R_w = 5.3%.

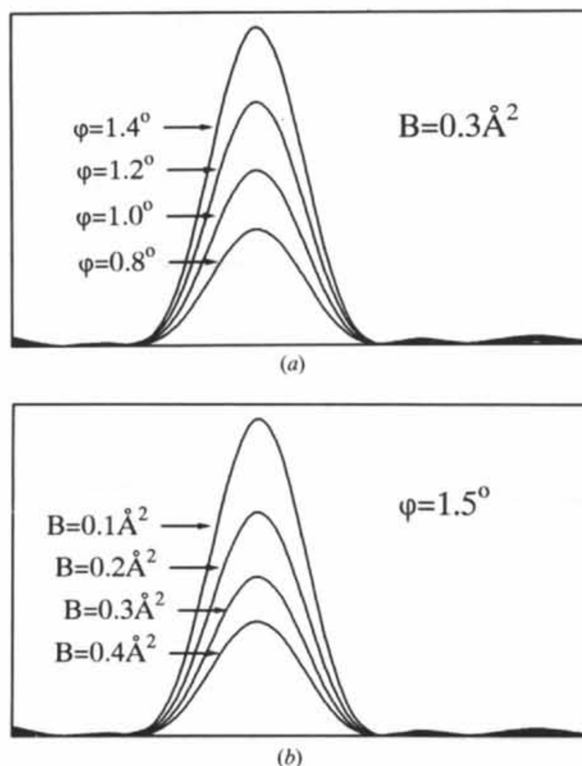

Fig. 5. Simulated line profiles of the 7,12,1 HOLZ reflection (*a*) for different φ and (*b*) for different B.

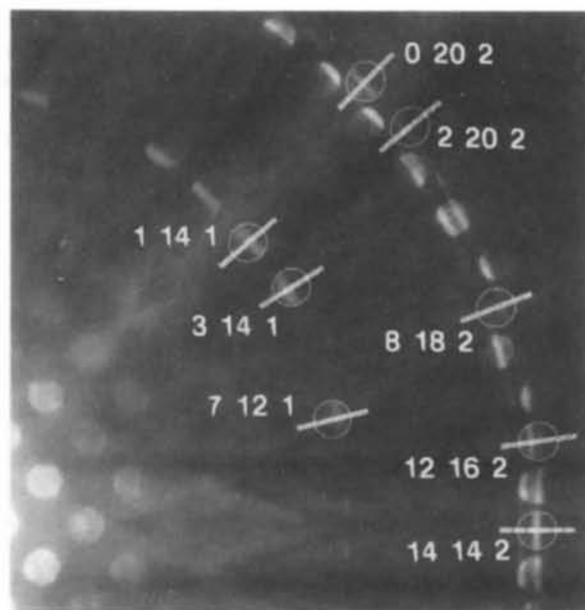

Fig. 6. The three FOLZ and five SOLZ reflections in Fig. 2 used for the analysis are indicated by circles. The FOLZ reflections are the superlattice reflections appearing only in the low-temperature phase.

Table 2. *Observed intensities, calculated (integrated) intensities and their residuals*

The R factors are $R = 8.2\%$ and $R_w = 5.3\%$.

h	k	l	Observed	Calculated	Residual
7	12	1	3.675	2.489	1.186
1	14	1	4.627	4.563	0.063
3	14	1	5.494	5.734	−0.240
14	14	2	8.518	8.501	0.017
8	18	2	1.675	2.405	−0.731
12	16	2	2.964	3.018	−0.054
0	20	2	4.458	4.429	0.029
2	20	2	1.000	1.353	−0.353

Fig. 7 shows the contour map of the residual sum of squares S with respect to the parameters φ and B. Since no local minimum is seen, it is confirmed that the values of the parameters obtained are the true solution corresponding to the global minimum of S.

3.5.2. *Case* II. *Line profiles.* Using the HOLZ line profiles, φ and B[O(2)] were determined so as to minimize S. The refined values were $\varphi = 1.14\,(1)^\circ$ and B[O(2)] $= 0.37\,(1)$ Å^2. This result agrees with the result from the integrated intensities within error. The number of total data points was 280, which was very much greater than the eight data points of the integrated intensities. As a result, the standard deviations of the refined parameters are greatly reduced. However, the deviations may be underestimated because the neighboring data points of the line profiles are too close to be independent of each other. Fig. 8 shows the final results of the fitting between experimental (+) and calculated (o) intensities. Calculated intensities are seen to agree well with experimental ones. However, the remaining small discrepancies give poor R factors of $R = 31.6\%$ and $R_w = 41.6\%$. These large values mainly originate from the errors in the distortion correction of the CBED pattern due to the aberrations of the lenses. For smaller R factors, it is therefore necessary to use lenses with small aberration coefficients and to correct the distortion of the CBED pattern due to the aberration more accurately.

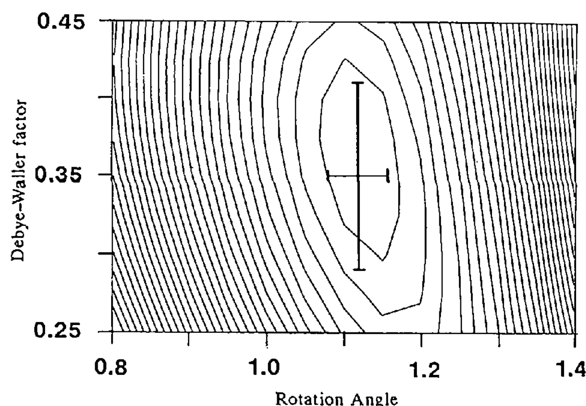

Fig. 7. Contour map of the residual sum of squares S with respect to parameters φ and B. The cross bar indicates the value obtained, $\varphi = 1.12\,(4)^\circ$ and B[O(2)] $= 0.35\,(6)$ Å^2. No local minimum is seen.

4. Discussion

4.1. *Comparison with other results*

Unoki & Sakudo (1967) and Müller, Berlinger & Waldner (1968) measured the rotation angle φ of the oxygen octahedron as a function of temperature over a temperature range from 4 to 105 K through electron spin resonance experiments. The former obtained the value of φ as $1.4\,(1)^\circ$ and the latter as 1.25° at 78 K. Shirane & Yamada (1969) determined φ to be $1.37\,(35)^\circ$ at 78 K from neutron diffraction experiments. Fujishita, Shiozaki & Sawaguchi (1979) determined φ to be $1.6\,(1)^\circ$ at 77 K from X-ray diffraction experiments. Fig. 9 shows these results together with the present ones. The present results shown by double circles are in good agreement with those of Unoki & Sakudo ($\varphi = 1.3^\circ$ at 87 K) and Müller *et al.* ($\varphi = 1.1^\circ$ at 87 K). The present results also agree with those of Shirane & Yamada when the temperature

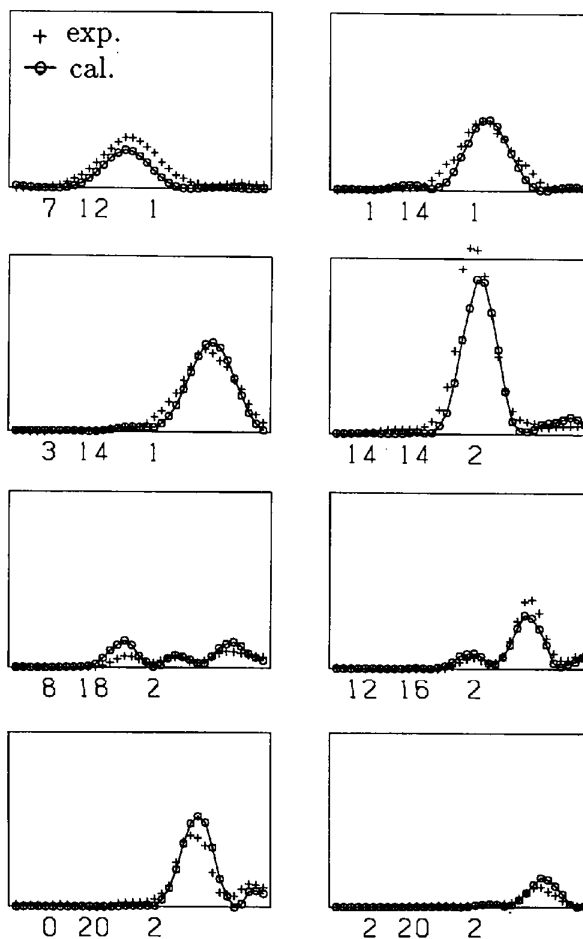

Fig. 8. Experimental (+) and calculated (o) line profiles. The parameters were determined to be $\varphi = 1.14\,(1)^\circ$ and B[O(2)] $= 0.37\,(1)$ Å^2.

difference is considered. The value obtained by Fujishita *et al.* is a little higher than the other results reported and may be a little different from ours even if the temperature difference is taken into account.

4.2. *Bloch states of* $SrTiO_3$

We interpret HOLZ line profiles in terms of Bloch waves (Kambe, Lehmpfuhl & Fujimoto, 1974; Buxton, 1976; Jones *et al.*, 1977; Buxton, Loveluck & Steeds, 1978). The high sensitivity of the reflections used in the present analysis to φ and B can be explained by the Bloch-wave picture as follows: The Bloch waves given by (5) are obtained as eigenstates of (4) for eigenvalues $k_0^{(j)}$. The eigenvalues $k_0^{(j)}$ for successively different incident directions form *dispersion surfaces*, whose sections are called *branches* 1, 2, . . . in order of the magnitude of their $k_0^{(j)}$. Fig. 10(*a*) shows the branches or the sections of the dispersion surfaces around the [001] incidence along the direction of the 5,19,2 reflection. The corresponding line profile of the 5,19,2 reflection is shown in Fig. 10(*b*). For simplicity, the surfaces of the eigenvalues were calculated using only one HOLZ reflection, 5,19,2, and 109 ZOLZ reflections. The branch originating from the HOLZ reflection is clearly distinguished from the branches due to ZOLZ reflections because the HOLZ branch makes a large angle with the ZOLZ branches, which are almost perpendicular to the [001] direction. The HOLZ and ZOLZ branches interact at their intersections and give rise to intensity peaks in the line profile of the HOLZ reflection. Then, each peak appearing in a HOLZ line profile can be assigned to a ZOLZ branch. Even if ZOLZ dispersion surfaces exist close together, the branches causing intensity peaks can be distinguished by examining values of the excitation amplitudes $\varepsilon^{(j)}$ of the Bloch waves. Only well excited branches cause peaks in a HOLZ line profile. The peaks of the line profile in Fig. 10(*b*) are assigned to those from branches 1, 2, 3 and 9. It is seen in Fig. 11(*a*) that $SrTiO_3$ consists of the Sr-atom rows, the Ti- and O(1)-atom rows and the O(2)-atom rows when viewed along the [001] direction. Figs. 11(*b*)–(*k*) show the electron-density distributions of the Bloch waves corresponding to branches 1–10, which were calculated using 109 ZOLZ beams at the [001] incidence for an accelerating voltage of 86 kV. The electron density is concentrated on the rows of Ti and O(1) atoms for branch 1 (Fig. 11*b*), on the rows of Sr atoms for branch 2 (Fig. 11*c*) and on the rows of O(2) atoms for branches 3 and 4 (Figs. 11*d* and *e*). Branches 3 and 4 correspond to a bonding state and an antibonding state between O(2) atoms, respectively. The wave functions at the neighboring O(2) atoms have the same sign in branch 3 but the opposite sign in branch

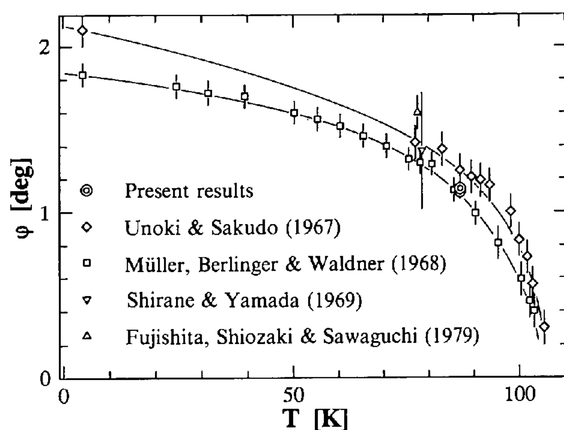

Fig. 9. Comparison of the present results (double circles) with other results.

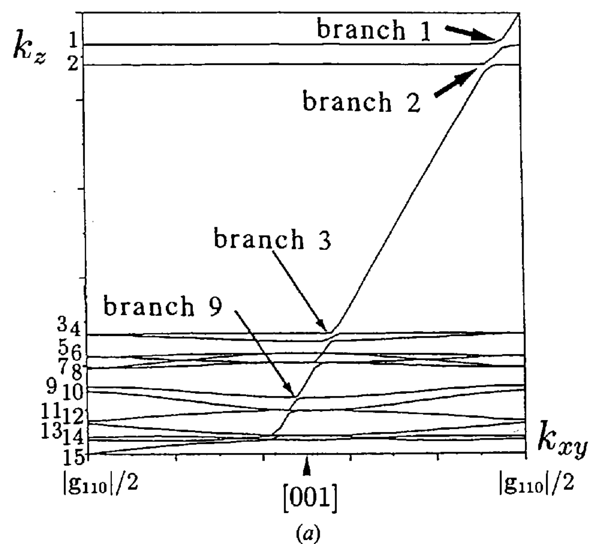

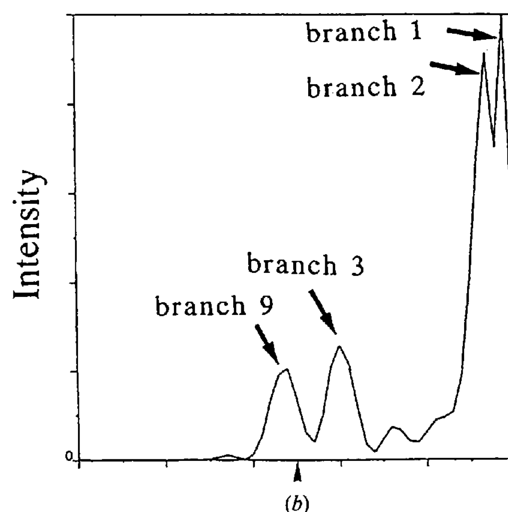

Fig. 10. (*a*) Branches of dispersion surfaces of $SrTiO_3$ around the [001] incidence. (*b*) The corresponding line profile of the 5,19,2 HOLZ reflection. Peaks of the line profile appear at the intersections of the HOLZ branch and the ZOLZ branches of 1, 2, 3 and 9.

4. The electron-density distribution of the Bloch waves resembles the two-dimensional atomic states localizing on the rows of particular atoms because the formulation of the dynamical theory is similar to the two-dimensional band theory of solid-state physics.

It should be noted that all the peaks appearing in the HOLZ reflections used in the present analysis (Fig. 8) originate only from branches 3 and 9, whose electron densities localize on the O(2) atoms. This is the reason why the HOLZ reflections are sensitive to the displacement of the O(2) atoms and their Debye–Waller factor.

5. Concluding remarks

We have proposed a CBED method to refine crystal structure parameters and demonstrated the usefulness of the method for the structure refinement of the low-temperature phase of $SrTiO_3$.

To improve the accuracy of the method, energy filtering to remove inelastic backgrounds is first required and the installation of image-forming lenses with small distortion is necessary. In the present analysis, the fitting parameters were limited to φ, B[O(2)] and the scale factor s to reduce the calculation time. It is necessary to add such parameters as lattice parameters, Debye–Waller factors of the other atoms [Sr, Ti and O(1)], the specimen thickness and low-order structure factors as the fitting parameters. The increase in calculation time with number of parameters can be compensated for by a perturbation method (Bird, 1990; Zuo, 1991) to calculate Jacobian matrices.

The maximum-entropy method (MEM) is worth applying to obtain directly crystal potential distributions from CBED patterns instead of determining the atom positions and the Debye–Waller factors in the present method.

We intend to determine the rotation angle φ of the oxygen octahedron of $SrTiO_3$ at the temperature of liquid helium and to apply the method to other substances that undergo structural phase transformations.

The authors are grateful to Dr K. A. Müller of IBM Zurich Research Laboratory, Switzerland, and Professor I. Hatta of Nagoya University, Japan, for providing the $SrTiO_3$ bulk crystals and to Dr M. Terauchi for preparation of the electron-microscope specimens. KT acknowledges financial support from Fellowships of

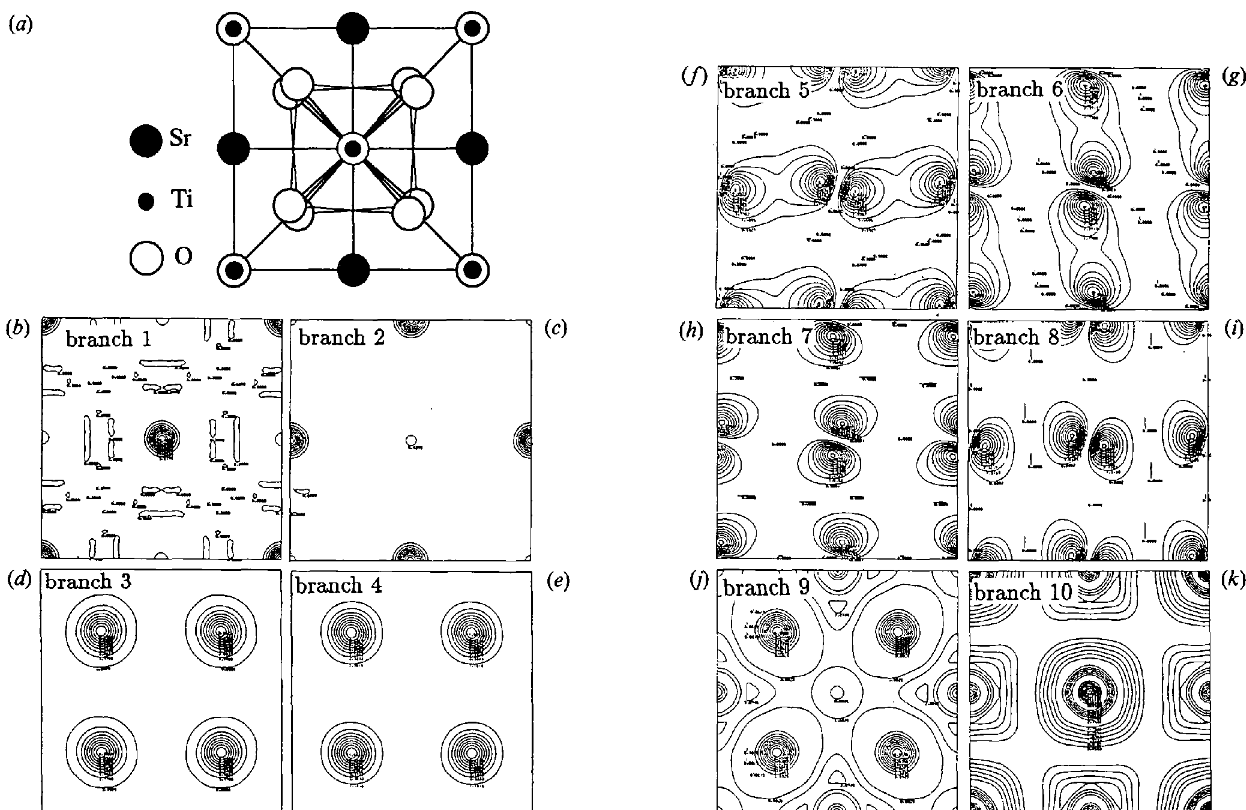

Fig. 11. (a) Projected structure of the low-temperature phase of $SrTiO^3$ along the [001] direction, (b)–(k) electron-density distributions of the Bloch waves of branches 1 to 10, respectively. It is noted that electron-density distributions of branches 3 (d), 4 (e) and 9 (j) are concentrated on the O(2) atoms.

the Japanese Society for the Promotion of Science for Japanese Junior Scientists. The present study was partly supported by a Grant in Aid of Scientific Research from the Ministry of Education, Science and Culture of Japan.

References

ALEFELD, B. (1969). *Z. Phys.* **222**, 155–164.

BENDERSKY, L. A. & KAUFMAN, M. J. (1986). *Philos. Mag.* B**53**, L75–L80.

BETHE, H. A. (1928). *Ann. Phys. (Leipzig)*, **87**, 55–129.

BIRD, D. M. (1990). *Acta Cryst.* A**46**, 208–214.

BIRD, D. M. & KING, Q. A. (1990). *Acta Cryst.* A**46**, 202–208.

BIRD, D. M. & SAUNDERS, M. (1991). *Microbeam Analysis*, edited by D. G. HOWITT, pp. 153–156. San Francisco Press.

BIRD, D. M. & SAUNDERS, M. (1992*a*). *Ultramicroscopy*, **45**, 241–251.

BIRD, D. M. & SAUNDERS, M. (1992*b*). *Acta Cryst.* A**48**, 555–562.

BUXTON, B. F. (1976). *Proc. R. Soc. London Ser. A*, **350**, 335–361.

BUXTON, B. F., EADES, J. A., STEEDS, J. W. & RACKHAM, G. M. (1976). *Philos. Trans. R. Soc. London*, **281**, 171–194.

BUXTON, B. F., LOVELUCK, J. E. & STEEDS, J. W. (1978). *Philos. Mag.* A**38**, 259–278.

COWLEY, J. M. & MOODIE, A. F. (1959). *Acta Cryst.* **12**, 360–367.

COWLEY, J. M., MOODIE, A. F., MIYAKE, S., TAKAGI, S. & FUJIMOTO, F. (1961). *Acta Cryst.* **14**, 87–88.

DORSET, D. L. (1992). *Ultramicroscopy*, **45**, 5–14, 357–364.

FLETCHER, R. (1971). *A Modified Marquardt Subroutine for Nonlinear Least Squares*, Harwell Report AERE-R 6799. Atomic Energy Research Establishment, Harwell, England.

FUJISHITA, H., SHIOZAKI, Y. & SAWAGUCHI, E. (1979). *J. Phys. Soc. Jpn*, **46**, 581–586.

GJØNNES, J., BOE, N. & GJØNNES, K. (1990). *Proc. XIIth ICEM*, edited by L. D. PEACHY & D. B. WILLIAMS, Vol. 2, pp. 516–517. San Francisco Press.

GJØNNES, J. & MOODIE, A. F. (1965). *Acta Cryst.* **19**, 65–67.

GJØNNES, K., GJØNNES, J., ZUO, J. & SPENCE, J. C. H. (1988). *Acta Cryst.* A**44**, 810–820.

GOODMAN, P. (1975). *Acta Cryst.* A**31**, 804–810.

GOODMAN, P. & LEHMPFUHL, G. (1964). *Z. Naturforsch. Teil A*, **19**, 818–820.

GOODMAN, P. & WHITEFIELD, H. J. (1980). *Acta Cryst.* A**36**, 219–228.

HALL, C. R. & HIRSCH, P. B. (1965). *Proc. R. Soc. London Ser. A*, **286**, 158–177.

HIRSCH, P. B., HOWIE, A., NICHOLSON, R. B., PASHLEY, D. W. & WHELAN, M. J. (1977). *Electron Microscopy of Thin Crystals*, 2nd ed., pp. 208–210. Florida: Krieger/London: Butterworth.

ICHIKAWA, M. & HAYAKAWA, K. (1977). *J. Phys. Soc. Jpn*, **42**, 1957–1964.

ISODA, S., SAITOH, K., MORIGUCHI, S. & KOBAYASHI, T. (1991). *Ultramicroscopy*, **35**, 329–338.

JONES, P. M, RACKHAM, G. M. & STEEDS, J. W. (1977). *Proc. R. Soc. London Ser. A*, **354**, 197–222.

KAMBE, K., LEHMPFUHL, G. & FUJIMOTO, F. (1974). *Z. Naturforsch. Teil A*, **29**, 1034-1044.

MARTHINSEN, K., HØIER, R. & BAKKEN, L. N. (1990). *Proc. XIIth ICEM*, edited by L. D. PEACHY & D. B. WILLIAMS, Vol. 2, pp. 492–493. San Francisco Press.

MAYER, J., SPENCE, J. C. H. & MÖBUS, G. (1991). *Proc. 49th Annu. Meet. EMSA*, edited by G. W. BAILEY, pp.786–787. San Francisco Press.

MIYAKE, S., TAKAGI, S. & FUJIMOTO, F. (1960). *Acta Cryst.* **13**, 360–361.

MOCHEL, M. E. & MOCHEL, J. M. (1986). *Proc. 44th Annu. Meet. EMSA*, pp. 616–617. San Francisco Press.

MOONEY, P. E., FAN, G. Y., MEYER, C. E., TRUONG, K. V. & KRIVANEK, O. L. (1990). *Electron Microscopy* 1990, *Proc.* XII*th ICEM*, edited by L. D. PEACHY & D. B. WILLIAMS, Vol. 1, pp. 164–165. San Francisco Press.

MORI, N., OIKAWA, T., HARADA, Y. & MIYAHARA, J. (1990). *J. Electron Microsc.* **39**, 437–443.

MORI, N., OIKAWA, T., KATO, T., MIYAHARA, J. & HARADA, Y. (1988). *Ultramicroscopy*, **25**, 195–207.

MÜLLER, K. A., BERLINGER, W. & WALDNER, F. (1968). *Phys. Rev. Lett.* **21**, 814–817.

NAKAGAWA, T. & OYANAGI, Y. (1980). *Recent Developments in Statistical Inference and Data Analysis*, edited by K. MATUSHITA. Amsterdam: North-Holland.

OIKAWA, T., MORI, N., TAKANO, N. & OHNISHI, M. (1990). *J. Electron Microsc.* **39**, 433–436.

REIMER, L. (1989). *Transmission Electron Microscopy*, 2nd ed., pp. 41–45. Berlin: Springer-Verlag.

SAITO, M., TANAKA, M., TSAI, A. P., INOUE, A. & MASUMOTO, T. (1992). *Jpn. J. Appl. Phys.* **31**, L109–L112.

SHIRANE, Y. & YAMADA, Y. (1969). *Phys. Rev.* **177**, 858–863.

SPENCE, J. C. H. (1993). *Acta Cryst.* **49**, 231–260.

STEEDS, J. W. & EVANS, N. S. (1980). *Proc. 38th Annu. Meet. EMSA*, pp. 188–191. San Francisco Press.

STEEDS, J. W., RACKHAM, G. M. & SHANNON, M. D. (1978). *Inst. Phys. Conf. Ser.* **41**, 135–139.

STIRLING, W. G. (1972). *J. Phys. C*, **5**, 2711–2730.

TAFTØ, T. & METZGER, T. H. (1985). *J. Appl. Cryst.* **18**, 110–116.

TANAKA, M. (1989). *J. Electron Microsc. Tech.* **13**, 27–39.

TANAKA, M. (1994). *Acta Cryst.* A**50**, 261–286.

TANAKA, M., SAITO, R. & SEKII, H. (1983). *Acta Cryst.* A**39**, 357–368.

TANAKA, M., SAITO, R. & TSUZUKI, K. (1982). *J. Phys. Soc. Jpn*, **51**, 2635–2640.

TANAKA, M., SAITO, R. & WATANABE, D. (1980). *Acta Cryst.* **36**, 350–352.

TANAKA, M., SEKII, H. & NAGASAWA, T. (1983). *Acta Cryst.* A**39**, 825–837.

TANAKA, M., SEKII, H. & OHI, K. (1985). *Jpn. J. Appl. Phys.* **24**, Supplement, pp. 814–816.

TANAKA, M. & TERAUCHI, M. (1985). *Convergent-Beam Electron Diffraction*. Tokyo: JEOL-Maruzen.

TANAKA, M., TERAUCHI, M., HIRAGA, K. & HIRABAYASHI, M. (1985). *Ultramicroscopy*, **17**, 279–286.

TANAKA, M., TERAUCHI, M. & KANEYAMA, T. (1988). *Convergent-Beam Electron Diffraction* II. Tokyo: JEOL-Maruzen.

TANAKA, M. & TSUDA, K. (1990). *Proc. XIIth ICEM*, edited by L. D. PEACHY & D. B. WILLIAMS, Vol. 2, pp. 518–519. San Francisco Press.

TANAKA, M. & TSUDA, K. (1991). *Proc. Microbeam Analysis*, edited by D. G. HOWITT, pp. 145–146. San Francisco Press.

TANAKA, M., TSUDA, K., TERAUCHI, M., FUJIWARA, A., TSAI, A. P., INOUE, A. & MASUMOTO, T. (1993). *J. Non-Cryst. Solids*, **153&154**, 98–102.

TERAUCHI, M. (1988). PhD thesis, Tohoku Univ., Japan. (In Japanese.)

TERAUCHI, M., TAKAHASHI, M. & TANAKA, M. (1994). *Acta Cryst.* A**50**, 566–574.

TERAUCHI, M. & TANAKA, M. (1993). *Acta Cryst.* A**49**, 722–729.

TOMOKIYO, Y. & KUROIWA, T. (1990). *Proc. XIIth ICEM*, edited by L. D. PEACHY & D. B. WILLIAMS, Vol. 2, pp. 526–527. San Francisco Press.

TSUDA, K., TANAKA, M. & AKIMITSU, J. (1989). *Jpn. J. Appl. Phys.* **28**, L1552–L1554.

TSUDA, K., TANAKA, M., SAKANOUE, J., SAWA, H., SUZUKI, S. & AKIMITSU, J. (1989). *Jpn. J. Appl. Phys.* **28**, L389–L391.

TSUNO, K. & HARADA, Y. (1981). *J. Phys. E*, **14**, 313–320, 955–960.

UNOKI, H. & SAKUDO, T. (1967). *J. Phys. Soc. Jpn*, **23**, 546–552.

VAINSHTEIN, B. K. (1956). *Structurnaya electronografiya*. Moscow: Izd. Akad. Nauk SSSR. (In Russian.)

VAINSHTEIN, B. K. (1964). *Structure Analysis by Electron Diffraction*. Oxford: Pergamon Press.

VAINSHTEIN, B. K., ZVYAGIN, B. B. & AVILOV, A. S. (1992). *Electron Diffraction Techniques*, Vol. 1, edited by J. M. COWLEY. Oxford Univ. Press.

VINCENT, R. & BIRD, D. M. (1986). *Philos. Mag.* A**53**, L35–L40.

VINCENT, R., BIRD, D. M. & STEEDS, J. W. (1984). *Philos. Mag.* A**50**, 745–763, 765–786.

VINCENT, R. & EXELBY, D. R. (1990). *Proc. XIIth ICEM*, edited by L. D. PEACHY & D. B. WILLIAMS, Vol. 2, pp. 524–525. San Francisco Press.

ZUO, J. M. (1991). *Acta Cryst.* A**47**, 87–95.

ZUO, J. M. & SPENCE, J. C. H. (1991). *Ultramicroscopy*, **35**, 185–196.

ZUO, J. M., SPENCE, J. C. H. & HØIER, R. (1989). *Phys. Rev. Lett.* **62**, 547–550.